

On the topological linkage of intertwined, spatial networks

Felix Kramer^{1,2,*} and Carl D. Modes^{1,2,3,†}

¹Max Planck Institute for Molecular Cell Biology and Genetics (MPI-CBG), Dresden 01307, Germany

²Center for Systems Biology Dresden (CSBD), Dresden 01307, Germany

³Cluster of Excellence, Physics of Life, TU Dresden, Dresden 01307, Germany

(Dated: 25. August 2022)

The observation, design and analysis of mesh-like networks in crystal chemistry, polymer physics and biological systems has brought forward an extensive catalog of fascinating structures of which a subgroup share a particular, yet critically under appreciated attribute: Intertwinedness. Here, intertwinedness describes the state of networks which are embedded in space such that one wouldn't be able to pull them apart without prior removal of a subset of edges. In this study we elaborate on a graph theoretical method to analyze the effective intertwinedness of any finite, 2-component nets on the basis of Hopf-link identification. Doing so we are able to construct an *edge priority* operator $\mathbf{\Lambda}$, derived from the linking numbers of the spatial graphs' cycle bases, which highlights critical edges for intertwinedness. On its basis we developed a greedy algorithm which identifies optimal edge removals to achieve unlinking, allowing for the establishment of a new topological metric characterizing spatial network intertwinedness.

How can one quantify intertwinedness? This question emerges throughout biology, chemistry and physics, e.g. when considering coiled DNA [1], compounds of vasculature [2, 3] or multi-component crystals [4–9]. It becomes particularly tricky when one has to distinguish two tangled objects from each other, for example by the number of cuts one has to perform to split the components. Naturally, this type of question has been extensively studied in the realm of knot theory [10, 11]. Yet, most work here has been performed on the characteristics of individual closed curves or intrinsic linking of one-component graph embeddings. While partial generalizations have been performed for extended meshes (and their graphical representations [12, 13]) much remains to be done for spatially embedded networks. With regard to multi-component biological systems we find to our best knowledge that no attempt has been made to characterize amorphous structures for intertwinedness with their environment. The mammalian liver lobule provides an illustrative example: here, intricate, intertwined sinusoid and bile canalicular networks are assumed to be crucial for the metabolic function of the organ [14]. Yet no useful measures of their intertwinedness exist.

We here develop a graph-theoretic framework which allows the identification of critical edges involved in the linkage of two spatially embedded networks. To achieve these means we introduce a linear operator, $\mathbf{\Lambda}$, which maps any two cycles (in edge-space representation) on to their respective linking number. This operator $\mathbf{\Lambda}$ quantifies a new form of edge priority, i.e. the importance of edges for the topological linkage of the system. We demonstrate that this allows for the efficient identification of minimal cuts between two linked structures. We

go on to further various network archetypes and conclude by discussing potential implications and applications of $\mathbf{\Lambda}$.

Recall that linking numbers, $l \in \mathbb{Z}$, are topological invariants which characterize the linking state (up to sign) of two closed curves, with $l = 0$ denoting the unlink and $l = \pm 1, \pm 2, \dots$ denoting linked states where the curves are not separable without breaking at least one of them [10], see Figure 1a. Given two closed, oriented curves with parametrizations $\gamma_1, \gamma_2 : [0, 1) \rightarrow \mathbb{R}^3$, their linking number is computable via the Gauss linking integral:

$$l(\gamma_1, \gamma_2) = \frac{1}{4\pi} \int_{\gamma_1} \int_{\gamma_2} (d\mathbf{r}_1 \times d\mathbf{r}_2) \cdot \frac{\mathbf{r}_1 - \mathbf{r}_2}{|\mathbf{r}_1 - \mathbf{r}_2|^3} \quad (1)$$

Note, the Gauss linking integral is a symmetric, bilinear mapping [10]. Thus a flip in the orientation of one curve $\gamma_i \rightarrow -\gamma_i$ will result in a sign change of the linking number as

$$l(-\gamma_1, \gamma_2) = -l(\gamma_1, \gamma_2) = l(\gamma_1, -\gamma_2) \quad (2)$$

One may further rewrite any closed curves as the composition of 'smaller' closed curves $\gamma_1 = \bigcup_{i=0}^n \sigma_{k_i} \gamma_{1k_i}$ (with canceling chords, see Figure 1b) with sub-orientations $\sigma_{k_i} = \pm 1$ and calculate its linking number as

$$\begin{aligned} l\left(\gamma_1 = \bigcup_{i=0}^n \sigma_{k_i} \gamma_{1k_i}, \gamma_2\right) & \\ &= \sum_{i=1}^{n_1} \frac{\sigma_{k_i}}{4\pi} \int_{\gamma_{1k_i}} \int_{\gamma_2} (d\mathbf{r}_{1k_i} \times d\mathbf{r}_2) \cdot \frac{\mathbf{r}_{1k_i} - \mathbf{r}_2}{|\mathbf{r}_{1k_i} - \mathbf{r}_2|^3} \\ &= \sum_{i=1}^{n_1} \sigma_{k_i} l(\gamma_{1k_i}, \gamma_2) \end{aligned} \quad (3)$$

Recall that a simple graph G is defined as a set of ver-

* kramer@mpi-cbg.de

† modes@mpi-cbg.de

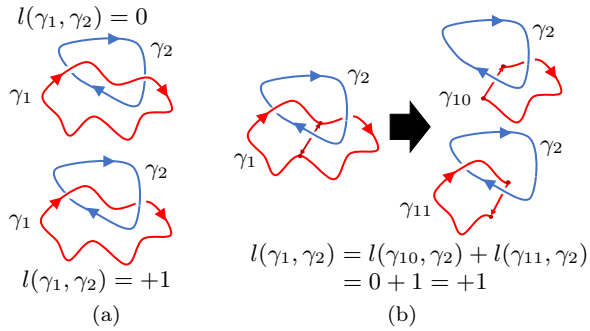


FIG. 1: Quantifying intertwinedness with linking numbers: (a) The invariant $l(\gamma_1, \gamma_2)$ characterizes the topological relation up to a sign, with $l = 0$ denoting the unlink and $l = \pm 1$ trivial links, e.g. the Hopf-link. (b) Chords (dark-red) allow for evaluation of $l(\gamma_1, \gamma_2)$ via the decomposition into subcurves.

tices, V , and edges, E . Further, there are two maps α, ω with $\alpha : E \rightarrow V$ and $\omega : E \rightarrow V$, uniquely defining each edge $e \in E$ as a tuple of vertices $(\alpha(e), \omega(e))$. Assuming $\alpha(e) \neq \omega(e)$ one can thereby define the edge's direction. A path is a sequence of such edges, while a cycle is a path, which starts and ends on the same vertex, traversing any of its edges only once. Fortunately one only need a certain subset of all possible cycles in a graph, the 'fundamental cycles', to construct the rest. One may identify these distinct cycles in the following way: Given a graph with one connected component of $|V|$ vertices and $|E|$ edges, a subset of $|V| - 1$ edges is sufficient to connect every vertex and thereby create a spanning tree. Therefore a set of non-utilized edges remains of cardinality

$$z = |E| - |V| + 1 \quad (4)$$

Adding any of these surplus edges to the tree will result in a fundamental cycle, which can be combined with with other such cycles to account for any possible loop in the graph. Note that z represents the dimension of the graph's cycle space (referred to as 'nullity' or the 'cyclomatic number' [15]), a vector space over \mathbb{Z}_2 with linear combinations achieved through edgewise XOR operations [16]. The astute reader may recognize this construction as the first homology of a chain complex composed of only 1-chains [17]. While this observation suggests an interesting path to generalization, as we are here focused on intertwinedness, we restrict ourselves in this letter to considering only space curves and network cycles, i.e. 1-chains. Further, as we are considering spatially embedded graphs, every node, edge and therefore path has a spatial curve representation. We thus use the decomposition of oriented closed curves into sub-curves for cycles in the spatial graphs considered, see Figure 2. Furthermore, one may derive matrices from graphs $G(V, E, \alpha, \omega)$ utilizing these topological characteristics, e.g. the 'mesh'

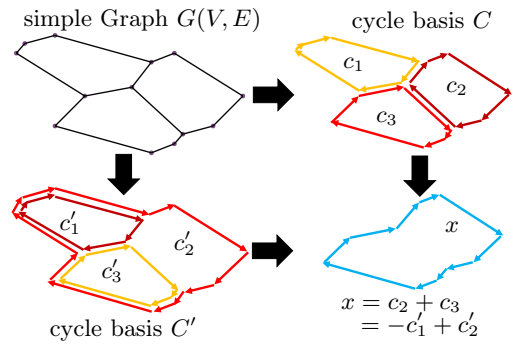


FIG. 2: Constructing arbitrary graph cycles from basis cycle superposition by oriented curve decomposition, as used in the path integrals of linking number calculations, see Figure 1 and Equation (6).

matrix typically encountered in electric circuits [18],

$$M_{ei} = \begin{cases} \pm 1 & \text{if cycle } i \text{ contains edge } e \\ 0 & \text{else} \end{cases} \quad (5)$$

The sign of M_{ei} captures the direction of the cycle with respect to the edge's direction. Note that z equals the rank of the mesh matrix \mathbf{M} , and that this operator transforms between the edge-space and cycle-space of a graph.

Let us consider cycle bases for two graphs as $C_1 = \{c_{11}, \dots, c_{1z_1}\}$ and $C_2 = \{c_{21}, \dots, c_{2z_2}\}$ and a polygonal representation via the respective graph's edges (piece-wise straight lines connecting the vertices). As previously shown, we may decompose any linking number calculation of arbitrary cycles c_1, c_2 in a graph pair as

$$l(c_1, c_2) = \sum_{i,j}^{z_1, z_2} \sigma_{1i} \sigma_{2j} l(c_{1i}, c_{2j}) \quad (6)$$

Or in terms of a linking number operator \mathbf{L} :

$$l(c_1, c_2) = \sigma_1^T \cdot \mathbf{L} \cdot \sigma_2 \quad (7)$$

$$\text{with } L_{ij} = l(c_{1i}, c_{2j}), \mathbf{L} \in \mathbb{Z}^{z_1 \times z_2}, \sigma_i \in \mathbb{Z}^{z_i}$$

Naturally, the linking numbers in this bilinear decomposition are invariant with respect to a change of the cycle basis, e.g. to C'_1 and C'_2 ,

$$\sigma_1^T \cdot \mathbf{L} \cdot \sigma_2 = \sigma_1'^T \cdot \mathbf{L}' \cdot \sigma_2' \quad (8)$$

demonstrating the independence to the choice of bases per graph. Next, we construct the invariant operator $\mathbf{\Lambda}$ which determines the importance of individual edges for the intertwinedness problem. Subsequently, we factorize \mathbf{L} using the mesh matrices \mathbf{M}_i of the respective networks (corresponding to the current basis),

$$\mathbf{L} = \mathbf{M}_1^T \cdot \mathbf{\Lambda} \cdot \mathbf{M}_2 \quad (9)$$

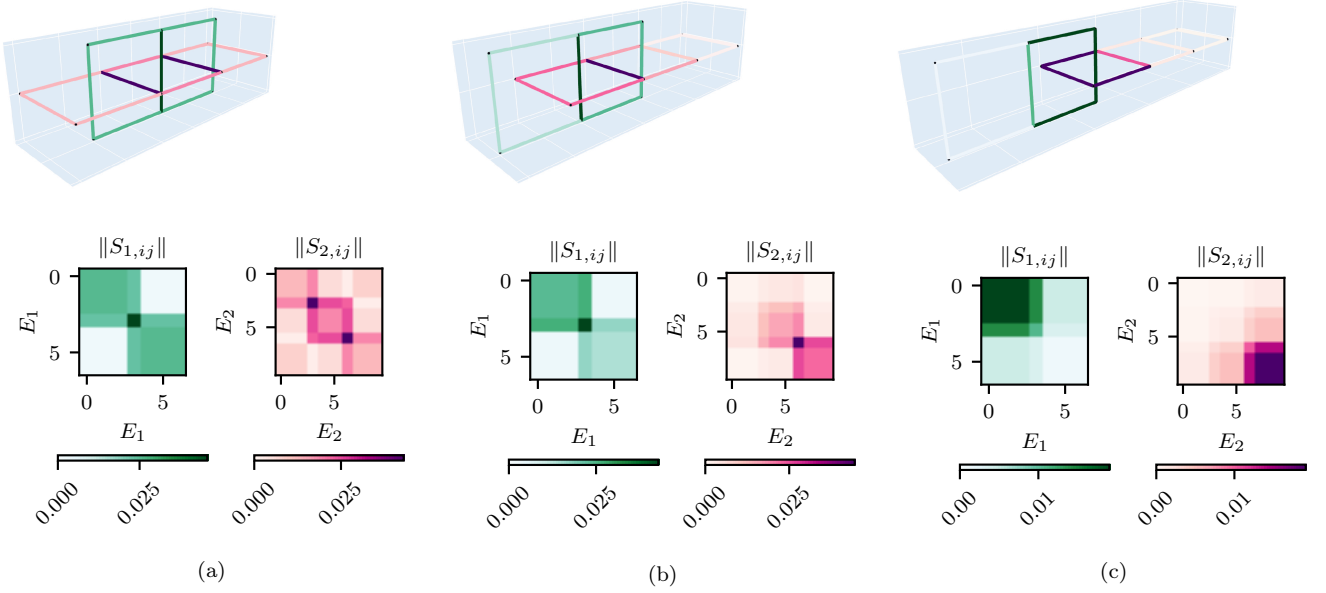


FIG. 3: Fully linked meshes unlink via axial translation. Top row: Visualization of simple meshes, color coded according to the diagonals of the corresponding priority operator \mathbf{S}_i . Bottom row: Heatmaps depicting the absolute values of priority operators \mathbf{S}_i for each mesh.

The matrix $\mathbf{\Lambda} \in \mathbb{R}^{E_1 \times E_2}$ is constructed via generalized inverses, as the mesh matrices do not have full rank:

$$\mathbf{\Lambda} = \left[\mathbf{M}_1^\dagger + \mathbf{X}_1 \cdot \mathbf{P}_1 \right]^T \cdot \mathbf{L} \cdot \left[\mathbf{M}_2^\dagger + \mathbf{X}_2 \cdot \mathbf{P}_2 \right] \quad (10)$$

with arbitrary factors $\mathbf{X}_i \in \mathbb{R}^{z_i \times E_i}$ and orthogonal projectors

$$\mathbf{P}_1 = \left[\mathbf{I} - \mathbf{M}_1 \mathbf{M}_1^\dagger \right] \quad \text{and} \quad \mathbf{P}_2 = \left[\mathbf{I} - \mathbf{M}_2 \mathbf{M}_2^\dagger \right] \quad (11)$$

These projectors signal a gauge freedom for $\mathbf{\Lambda}$ as they satisfy $\mathbf{P}_i \mathbf{M}_i = 0$. Here we choose the least square solution as the canonical form:

$$\mathbf{\Lambda}_0 \equiv \mathbf{M}_1^{\dagger, T} \cdot \mathbf{L} \cdot \mathbf{M}_2^\dagger \quad (12)$$

We may then rewrite the linking number of two arbitrary cycles in a graph pair as

$$l(c_1, c_2) = \boldsymbol{\sigma}_1^T \cdot \mathbf{M}_1^T \cdot \mathbf{\Lambda}_0 \cdot \mathbf{M}_2 \cdot \boldsymbol{\sigma}_2 \quad (13)$$

where we know the edge representation of the cycles to be

$$\mathbf{p}_1^T = \boldsymbol{\sigma}_1^T \cdot \mathbf{M}_1^T \quad \text{and} \quad \mathbf{p}_2 = \mathbf{M}_2 \cdot \boldsymbol{\sigma}_2 \quad (14)$$

with $\mathbf{p}_i \in K^{E_i}$, where $K = \{-1, 0, 1\}$. Thus we may write the linking number of any two cycles in the intertwined system in edge-space form as

$$l(c_1, c_2) = \mathbf{p}_1^T \cdot \mathbf{\Lambda}_0 \cdot \mathbf{p}_2 \quad (15)$$

The meaning of $\mathbf{\Lambda}_0$ becomes more apparent if we consider

the symmetric constructions of the positive definite operators $\mathbf{S}_1 = \mathbf{\Lambda}_0 \mathbf{\Lambda}_0^T \in \mathbb{R}^{E_1 \times E_1}$ and $\mathbf{S}_2 = \mathbf{\Lambda}_0^T \mathbf{\Lambda}_0 \in \mathbb{R}^{E_2 \times E_2}$. We focus on these operators in particular as they allow the evaluation of the impact of edges on non-zero linking numbers. We refer to the diagonals of \mathbf{S}_i as the *priority* of edges, see appendix A for further detail.

As an illustration of the concept, consider a dual ladder graph system, see Figure 3. We display the changes in \mathbf{S}_i while separating the graphs in discrete translational steps. The plots show the respective edge priorities, the visualization of the respective diagonals of \mathbf{S}_i . Note that priorities are at their maximum for the most central ladder legs, corresponding to the edges which must be traversed by any linked cycle. As the graphs are separated one observes a shift of edge priorities in both graphs as different edges become crucial connections through which any linked cycle must pass. A complete spatial separation of the networks naturally results in the \mathbf{S}_i becoming null operators as no link remains. One may therefore characterize any intertwined system by a hierarchical ordering of edge priorities, indicating the crucial topological links in both graphs. Such a scheme may be used to determine the optimal cut between two meshes, i.e. *how many and which edges* ε one has to remove from either graph such that the entire system becomes unlinked.

We propose the following simple algorithm to identify such a cut set: Given two graphs G_1 and G_2 , set one as a reference graph G_{ref} and the other as a target graph G_{target} . Then compute the linkage matrix \mathbf{L} as described before and the edge space operators $\mathbf{\Lambda}_0$, \mathbf{S}_{ref} and \mathbf{S}_{target} . Next, identify the maximum priority on the diagonal of \mathbf{S}_{target} and remove the corresponding edge from G_{target} . Iterate on the linking number evaluation

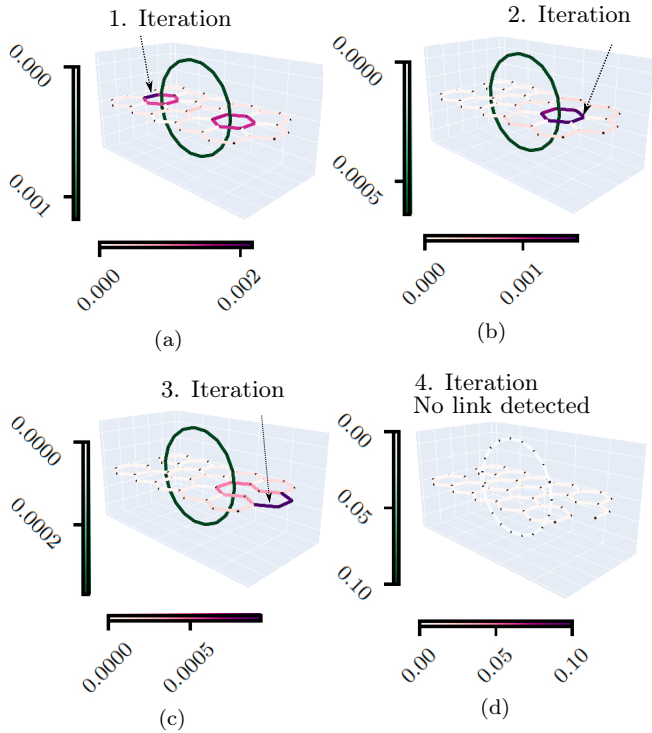


FIG. 4: Greedy edge cutting algorithm: Example of a single ring linked to a hexagonal mesh, unlinked in 4 iterations. Displayed is the momentary optimal cut, based on highest edge priority.

and the edge removal until the linking number calculation generates null-matrices, indicating the unlink of the original meshes G_1, G_2 . Doing so yield a list of edges in the target graph representing a cut set of cardinality ε_{target} .

Despite the fact that this is a greedy algorithm, we found it to reliably identify efficient cuts between two meshes, independent of their particular embedding and graph topology, as for example demonstrated for the Hopf-linked hexagonal grid in Figure 4. Further, we are not only able to identify which edges to remove to break the topological linkage, we are also able to account for asymmetries and redundancies in the intertwinedness. Note though that we only consider the edges of highest priority during each iteration, which may lead to cuts not representative of the global optimum. Such inaccuracies occur when meshes have links close to their periphery, leading to high edge priorities in this section which may obscure better cuts. For example, in Figure 4, there is an equally efficient cut set found by removing the edges from the hexagonal grid passing the rings cross-section, yet edges on the periphery of the hexagon have higher priorities.

This algorithm also suggests an associated intertwinedness metric. Subsequently let us refer to the cardinality of cuts for any mesh G_i as ε_i and compare it to the cyclomatic number z_i . We accordingly define the relative

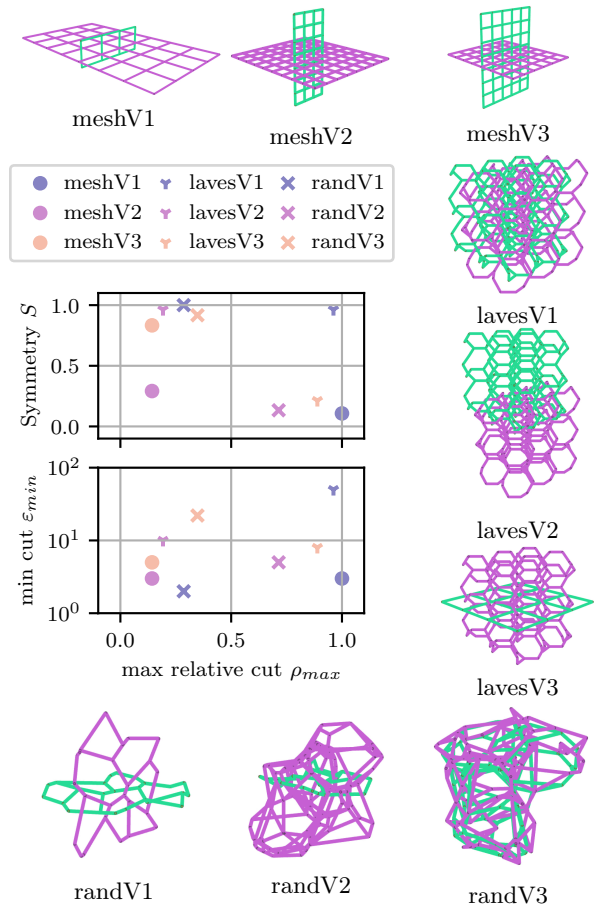


FIG. 5: Classification of entangled systems: Maximum relative cut number ρ_{max} (17) and linkage asymmetry S (18) present a system's redundancy and asymmetry, while the mutual cut coefficient ε_{min} (19) being the minimal number of cuts between the two systems.

cut number as

$$\rho_i \equiv \frac{\varepsilon_i}{z_i} \quad (16)$$

accounting for how much of a network's cycle space has to be taken down before the unlinking event, i.e. if $\rho_i = 1$ every single cycle in a mesh has to be eliminated. The trivial case of $z_i = 0$ simply implies that at least one of the networks is a tree, and therefore not topologically linked by default. This metric classifies networks according to their basis utilization, indicating whether a network has a bloated cycle space which does not significantly contribute to the linkage of the system. As one typically has no preference for either of the two meshes involved we utilize the following order parameters:

$$\rho_{max} = \max(\rho_1, \rho_2) \quad (17)$$

$$S = \frac{\min(\rho_1, \rho_2)}{\rho_{max}} \quad (18)$$

These two parameters effectively allow us to distinguish different intertwined mesh systems on the basis of their

effective cycle space utilization as well as their linkage symmetry. These tools, however miss size-dependent effects. To address this, we define the minimal cut coefficient,

$$\varepsilon_{min} = \min(\varepsilon_1, \varepsilon_2) \quad (19)$$

which accounts for the actual number of cuts one has to perform before the system splits. This order parameter is thus sensitive the size of the intertwined system. We highlight the strength of this method in Figure 5, where we survey a small set of intertwined archetypes, i.e. finite spatially embedded graphs (either planar or non-planar) with different kinds of cycle space utilization. Note that our metric is sensitive to translations of highly symmetrical lattices ('Laves' examples) as well as to random spatial structures ('rand' examples), while being able to distinguish networks of equal cut numbers in terms of cycle space utilization and symmetry ('mesh' examples).

We have demonstrated a new classification tool for intertwined spatial networks, by combining conventional methodologies of graph topology, mesh matrices and linking number integrals. This allows for effective surveys of intertwined networks on the basis of Hopf link identification and provides the means to classify different redundancies and symmetries in such meshes. Note, that this approach is unfortunately unable to identify higher order

links such as Brunnian entanglements [19]. Possibly, one could extend the method to include these cases by utilizing Milnor coefficients [20]. Nevertheless we would point to applicability of this approach to vessel systems in developmental and pathological biology, as the liver lobule presents a model to be more thoroughly tested, e.g. for zonation effects, see appendix B. Naturally this could also be deployed with regard to other organs such as kidney, pancreas and the lymphatic system or optimized transport networks more generally, see appendix C. Furthermore, as connectome mapping matures, there is mounting evidence for spatial intertwining among neural subcircuits, presenting another intriguing potential application [21].

We therefore envision this approach to enable a new kind of spatial network analysis, by taking the topological consequences of embedding into account.

ACKNOWLEDGMENTS

We would like to dearly thank the members of the Zerial-lab (MPI-CBG) for providing us with experimental data and expertise to analyze liver lobule structures. We would further like to thank the members of the Modes and Zechner-lab (CSBD) for feedback and criticism during the creation of the manuscript. In particular we would like to thank Szabolcs Horvat and Carlos Duque for their advice during the research phase.

-
- [1] B. I. Murasugi, Kunio Kurpita, *Modern Birkhäuser Classics*, reprint of the 1996 ed. ed. (Birkhäuser, Boston, 2008).
- [2] F. Kramer and C. D. Modes, How to pare a pair: Topology control and pruning in intertwined complex networks, *Physical Review Research* **2**, [10.1103/PhysRevResearch.2.043171](https://doi.org/10.1103/PhysRevResearch.2.043171) (2020).
- [3] B. Grigoryan, S. J. Paulsen, D. C. Corbett, D. W. Sazer, C. L. Fortin, A. J. Zaita, P. T. Greenfield, N. J. Calafat, J. P. Gounley, A. H. Ta, F. Johansson, A. Randles, J. E. Rosenkrantz, J. D. Louis-Rosenberg, P. A. Galie, K. R. Stevens, and J. S. Miller, Multivascular networks and functional intravascular topologies within biocompatible hydrogels, *Science* **364**, 458 (2019).
- [4] S. C. Power, I. A. Baburin, and D. M. Proserpio, Isotopy classes for 3-periodic net embeddings, *Acta Crystallogr A Found Adv* **76**, 275 (2020).
- [5] C. Bonneau and M. O’Keeffe, High-symmetry embeddings of interpenetrating periodic nets. essential rings and patterns of catenation, *Acta Crystallogr A Found Adv* **71**, 82 (2015).
- [6] S. T. Hyde and O. D. Friedrichs, From untangled graphs and nets to tangled materials, *Solid State Sciences* **13**, 676 (2011).
- [7] K. E. Horner, M. A. Miller, J. W. Steed, and P. M. Sutcliffe, Knot theory in modern chemistry, *Chem Soc Rev* **45**, 6432 (2016).
- [8] R. S. Forgan, J. P. Sauvage, and J. F. Stoddart, Chemical topology: complex molecular knots, links, and entanglements, *Chem Rev* **111**, 5434 (2011).
- [9] S. R. Batten, Topology of interpenetration, *CrystEng-Comm* **3**, [10.1039/b102400k](https://doi.org/10.1039/b102400k) (2001).
- [10] D. Rolfsen, *Knots and Links* (AMS Chelsea Publishing, 1976).
- [11] J. H. Conway and C. M. Gordon, Knots and links in spatial graphs, *Journal of Graph Theory* **7**, 445 (1983).
- [12] C. E. Soteros, D. W. Summers, and S. G. Whittington, Entanglement complexity of graphs in \mathbb{Z}^3 , *Mathematical Proceedings of the Cambridge Philosophical Society* **111**, 75 (2008).
- [13] T. Castle, M. E. Evans, and S. T. Hyde, Ravels: knot-free but not free. novel entanglements of graphs in 3-space, *New Journal of Chemistry* **32**, [10.1039/b719665b](https://doi.org/10.1039/b719665b) (2008).
- [14] H. Morales-Navarrete, F. Segovia-Miranda, P. Klukowski, K. Meyer, H. Nonaka, G. Marsico, M. Chernykh, A. Kalaidzidis, M. Zerial, and Y. Kalaidzidis, A versatile pipeline for the multi-scale digital reconstruction and quantitative analysis of 3d tissue architecture, *Elife* **4**, [10.7554/eLife.11214](https://doi.org/10.7554/eLife.11214) (2015).
- [15] H. Whitney, Non-separable and planar graphs, in *Hasler Whitney Collected Papers*, edited by J. Eells and D. Toledo (Birkhäuser Boston, Boston, MA, 1992) pp. 37–59.
- [16] C. D. Modes, M. O. Magnasco, and E. Katifori, Extracting hidden hierarchies in 3d distribution networks, *Physical Review X* **6**, [10.1103/PhysRevX.6.031009](https://doi.org/10.1103/PhysRevX.6.031009) (2016).

- [17] N. Otter, M. A. Porter, U. Tillmann, P. Grindrod, and H. A. Harrington, A roadmap for the computation of persistent homology, [EPJ Data Sci](#) **6**, 17 (2017).
- [18] C. A. Desoer and E. S. Kuh, *Basic circuit theory* (McGraw-Hill, New York [u.a.], 1969).
- [19] L. Carlucci, G. Ciani, D. M. Proserpio, T. G. Mitina, and V. A. Blatov, Entangled two-dimensional coordination networks: a general survey, [Chem Rev](#) **114**, 7557 (2014).
- [20] J. Milnor, Isotopy of links, in *Algebraic Geometry and Topology: A Symposium in Honor of Solomon Lefschetz*, edited by R. H. Fox (Princeton University Press, 2015) pp. 280–306.
- [21] M. W. Moyle, K. M. Barnes, M. Kuchroo, A. Gonopolskiy, L. H. Duncan, T. Sengupta, L. Shao, M. Guo, A. Santella, R. Christensen, A. Kumar, Y. Wu, K. R. Moon, G. Wolf, S. Krishnaswamy, Z. Bao, H. Shroff, W. A. Mohler, and D. A. Colón-Ramos, Structural and developmental principles of neuropil assembly in *c. elegans*, [Nature](#) **591**, 99 (2021).
- [22] K. Si-Tayeb, F. P. Lemaigre, and S. A. Duncan, Organogenesis and development of the liver, [Dev Cell](#) **18**, 175 (2010).
- [23] K. Meyer, O. Ostrenko, G. Bourantas, H. Morales-Navarrete, N. Porat-Shliom, F. Segovia-Miranda, H. Nonaka, A. Ghaemi, J. M. Verbavatz, L. Brusch, I. Sbalzarini, Y. Kalaidzidis, R. Weigert, and M. Zerial, A predictive 3d multi-scale model of biliary fluid dynamics in the liver lobule, [Cell Syst](#) **4**, 277 (2017).
- [24] H. Morales-Navarrete, H. Nonaka, A. Scholich, F. Segovia-Miranda, W. de Back, K. Meyer, R. L. Bogorad, V. Kotliansky, L. Brusch, Y. Kalaidzidis, F. Julicher, B. M. Friedrich, and M. Zerial, Liquid-crystal organization of liver tissue, [Elife](#) **8**, 10.7554/eLife.44860 (2019).
- [25] J. Karschau, A. Scholich, J. Wise, H. Morales-Navarrete, Y. Kalaidzidis, M. Zerial, and B. M. Friedrich, Resilience of three-dimensional sinusoidal networks in liver tissue, [PLoS Comput Biol](#) **16**, e1007965 (2020).
- [26] L. D. Landau and E. M. Lifshitz, *Course of theoretical physics / L. D. Landau and E. M. Lifshitz ; 6*, 2nd ed. (Elsevier Butterworth-Heinemann, Amsterdam, 2007).
- [27] F. Corson, Fluctuations and redundancy in optimal transport networks, [Phys Rev Lett](#) **104**, 048703 (2010).
- [28] D. Hu and D. Cai, Adaptation and optimization of biological transport networks, [Phys Rev Lett](#) **111**, 138701 (2013).
- [29] F. Kramer and C. D. Modes, [On biological flow networks: Antagonism between hydrodynamic and metabolic stimuli as driver of topological transitions](#) (2021).

Appendix A: From circuits to linkages

This appendix is intended to detail the derivation of the edge priority operator Λ_0 . First let us re-introduce the mesh matrix M , which was defined in (5), and is commonly used in linear circuit theory [18]. The mesh matrix M (also fundamental loop -, circuit -, tie set matrix) indicates which edges are involved in which of cycle in a graph. It also provides us with the possibility to project any vectors of the cycle space on to the edge space as

$$M \cdot \sigma = p \quad (\text{A1})$$

In terms of circuit theory one interprets σ as a vector of mesh currents and p the vector of edge currents. The mesh impedance for a network with homogeneous edge resistance (equal to one) is further calculated as

$$Z = M^T \cdot M \quad (\text{A2})$$

Now, let us turn toward the interpretation of $\Lambda_0^T \Lambda_0$ and $\Lambda_0 \Lambda_0^T$ as we calculate these as

$$\Lambda_0 \Lambda_0^T = M_1^{\dagger, T} \cdot L \cdot M_2^{\dagger} M_2^{\dagger, T} \cdot L^T \cdot M_1^{\dagger} \quad (\text{A3})$$

$$\Lambda_0^T \Lambda_0 = M_2^{\dagger, T} \cdot L^T \cdot M_1^{\dagger} M_1^{\dagger, T} \cdot L \cdot M_2^{\dagger} \quad (\text{A4})$$

Now as the impedance matrices $Z_i = M_i^{\dagger} M_i^{\dagger, T}$ are actually invertable we may rewrite this as

$$S_1 = M_1^{\dagger, T} \cdot L \cdot Z_2^{-1} \cdot L^T \cdot M_1^{\dagger} \quad (\text{A5})$$

$$S_2 = M_2^{\dagger, T} \cdot L^T \cdot Z_1^{-1} \cdot L \cdot M_2^{\dagger} \quad (\text{A6})$$

As the networks (and their loops) get larger in terms of edges per path, one can readily see that the effective mesh conductivity Z_i^{-1} decreases. Remember, that L denotes the linkage matrix of the respective fundamental loop sets. In comparison with electric circuits one may interpret the linking numbers $L_{ij} \neq 0$ as mutual inductance (usually denoted as M [18]) of coupled coils, with $L_{ij} = 0$ corresponding to completely uncoupled elements. Note, that one may need to call it mutual inductance rate actually for the analogy's sake, as it would need to correspond to the change in current for further circuit comparisons. With that in mind, the vector

$$\mathbf{u}_1 = L M_2^{\dagger} \mathbf{p}_2 \quad (\text{A7})$$

$$\mathbf{u}_2 = L^T M_1^{\dagger} \mathbf{p}_1 \quad (\text{A8})$$

would correspond to the loop voltage vector (via mutual inductance of coupled coils).

So how does this help us understand S_i ? Well, one may interpret any scalar $P_i = \mathbf{p}_i^T \cdot S_i \cdot \mathbf{p}_i$ as a power dissipation in the circuit analogy as we may write

$$P_1 = \mathbf{p}_1^T \cdot S_1 \cdot \mathbf{p}_1 = \mathbf{u}_2^T \cdot Z_2^{-1} \cdot \mathbf{u}_2 \quad (\text{A9})$$

$$P_2 = \mathbf{p}_2^T \cdot S_2 \cdot \mathbf{p}_2 = \mathbf{u}_1^T \cdot Z_1^{-1} \cdot \mathbf{u}_1 \quad (\text{A10})$$

Note that this would denote the power dissipation of currents in the respective partner networks. Therefore we expect diagonal elements of S_i (corresponding to graph edges) to decay to zero if:

1. the respective edges stop being a part of a coupled loop, e.g. as part of a translation of the graphs, altering topological linkage
2. number of constituting edges in the loops (thereby the impedance) in the partner network is increased

Appendix B: Analyzing model systems I - Intertwined vasculature in liver acinus

The characterization techniques presented in this study were, partially, inspired by biological model systems, mainly those found in the liver lobule (one of the fundamental tissue elements in the liver [22]). Here, sinusoids (blood vessels, endothelial tissue) and bile canaliculi (ducts for waste removal and digestive components, epithelial tissue) form an intricate, yet spatially separate, network system displaying a manifold of interesting features for a transport system [23–25]. Utilizing a data set from previous analysis [2], we focus on a small section of tissue found in the liver acinus, an element between the central vein and a portal triad, see Figure 6a. Due to the segmentation techniques of the collaborators (Zerial Lab, MPI-CBG Dresden) who provided us with these data, we further have the relative positional information of vessel pieces in the acinus [14], i.e. we know which part of the network is close to the central vein (denoted as $\chi = 0$) and which is most distant ($\chi = 1000$). As it is usually of interest how the properties of liver tissue change with regard to its relative distance to the central vein/ portal triad, we perform an analysis of the linkage behavior as follows: We compartmentalize sections of the mesh system with regard to $\Delta\chi = 150$ intervals, see Figure 6b to 6g. Subsequently we analyze the linkage of the partial mesh systems in accordance to minimal cut numbers ε_{min} , symmetries S and effective cycle utilization ρ_{max} . Needless to say, interval size of $\Delta\chi$ will influence the detected linkage behavior, as well as the generation of artifacts (say the creation of multiple connected components, and broken loops). We shall focus here on the largest connected component and prune it (remove all leaves) before further analysis. In Figure 7 we display the results for zonation differentiated linkage. One may see that this system shows a wide range of linkage symmetry S throughout the entire acinus, with severe fluctuations towards the central vein. Furthermore it seems one observes a rather constant overall utilization of the cycle space ρ_{12} throughout the acinus, which is interesting as the minimal cut numbers decrease significantly when getting closer to the central vein. The proposed cutting algorithm and priority computation indicates a useful tool for characterization of zoned intertwined, yet we find that further, more comprehensive studies are in order.

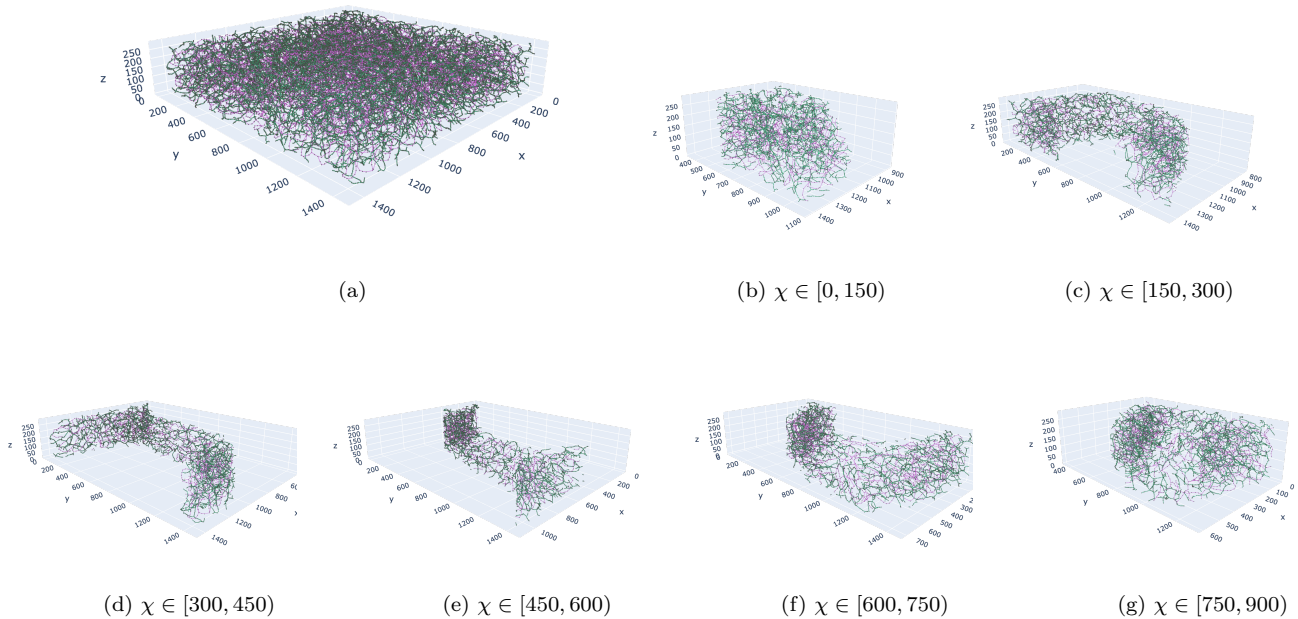


FIG. 6: Network skeletons of liver tissue vasculature: (a) Sinusoids (magenta) and bile canaliculi (green) segment in the liver acinus. (b) - (g) Separation of the vasculature mesh into regular $\Delta\chi = 150$ sections.

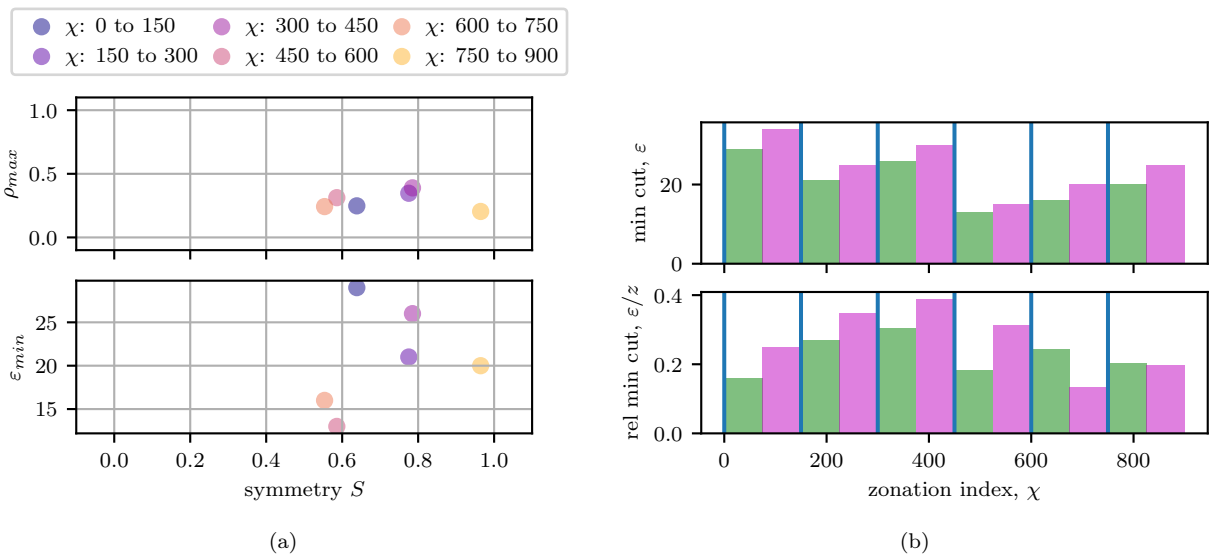


FIG. 7: Classification of entangled systems in the liver lobule for $\Delta\chi = 150$ compartmentalization: (a) Minimal cut numbers and linkage parameters for liver network segments in the acinus. (b) Zonation and network differentiated overview of minimal cut numbers and cycle space utilization

Appendix C: Analyzing model systems II - Optimized transport networks

In this section we present a linkage analysis of intertwined adapting, insilico transport networks, which represent

another toy model used for capillary systems [2]. The transport networks of interest are modeled as Kirchhoff networks, i.e. allowing us to utilize a lumped parameter model with flows f as direct linear response to potential differences Δp , e.g. a Hagen-Poiseuille law [26]

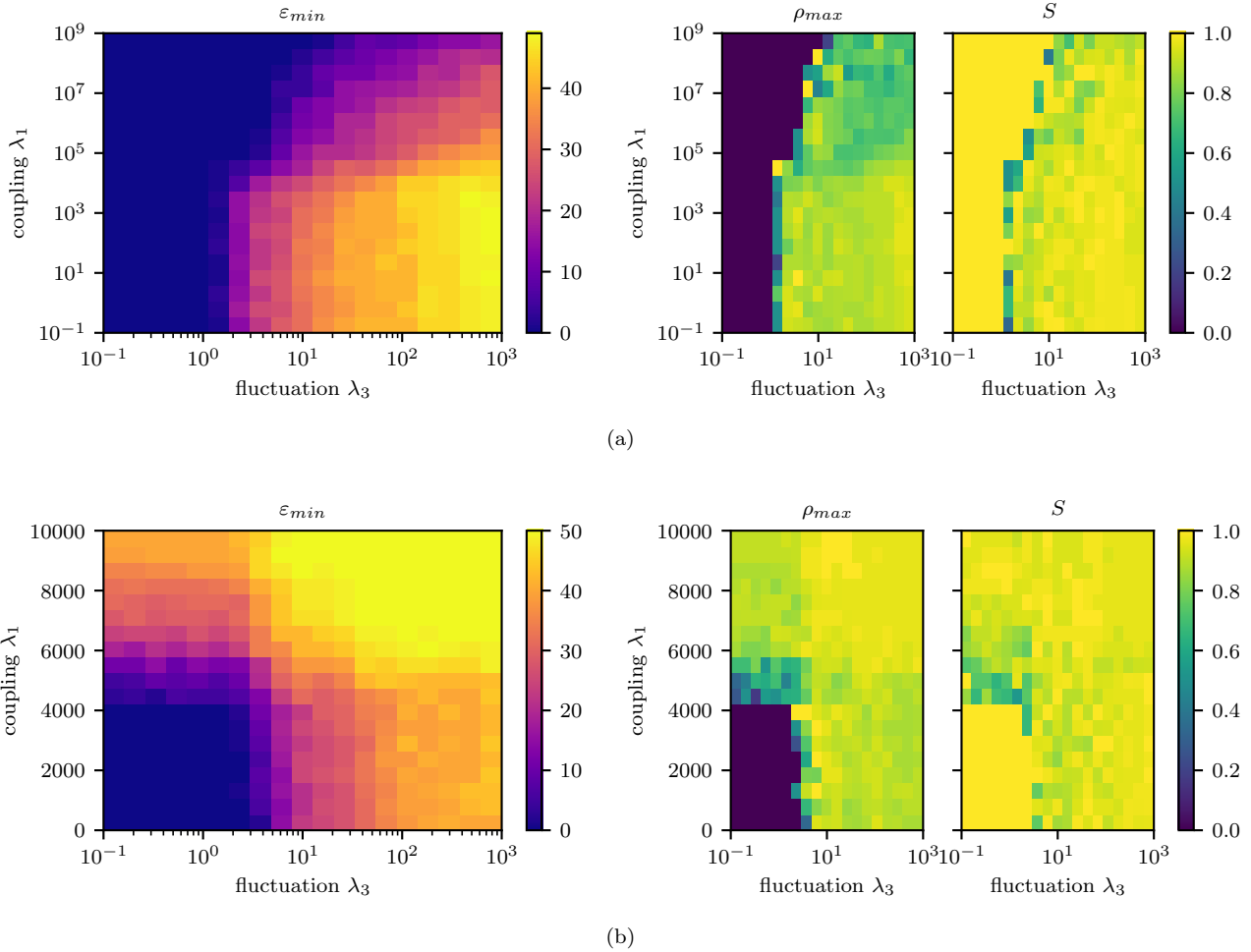


FIG. 8: Classification of entangled, adapting and (a) repulsively coupled systems ($\nu > 1$) as well as (b) attractively coupled systems ($\nu < -1$) systems.

$f_e = \frac{\pi r_e^4 \Delta p_e}{8\eta_e l_e}$ and $\sum_e B_{en} f_e = s_n$ for all edges e and nodes n . Here edges in the network are assigned a length l , a local fluid viscosity η and vessel radii r and the graphs incidence matrix B_{en} . In [2] one defines a multilayer network consisting of two intertwined, yet spatially separate meshes. Here we perform all simulation on 'laves3' systems, i.e. see the mesh 'lavesV1' in Figure 5, with sources placed in spatially opposing corners of the networks. This model incorporates affiliation of edges: Given a minimal cycle (no chords or further deconstruction into smaller cycles possible) in a network we say that all its composing edges are affiliated with edges of other other cycles linked with the former one. As all edges are simply tubes in our model, we have the distance between affiliated tubes defined as,

$$\Delta r_{ee'} = L - (r_e + r_{e'}) \quad (\text{C1})$$

where L is the initial distance of the skeletons (equal to distance in case of simultaneously vanishing radii). Hence

one describes this relationship between the edges e, e' as

$$F_{ee'} = \begin{cases} 1 & \text{if edges } e \text{ and } e' \text{ affiliated} \\ 0 & \text{else} \end{cases} \quad (\text{C2})$$

As discussed in [27] one finds sink-source fluctuations to be a crucial component in transport network adaption. We only consider s -configurations in which there exists one source-node (here $j = 0$) and all other nodes being sinks with the following characteristics:

$$\langle s_j \rangle = \mu \text{ with } j > 0 \quad (\text{C3})$$

$$\langle s_j s_k \rangle = q_{jk} \sigma^2 + \mu^2 \text{ with } j, k > 0 \quad (\text{C4})$$

Hence one may compute the effective pressure response $\langle \Delta p_e \rangle$ for any individual edge. Eventually we utilize an adaption scheme of edge radii in either network in response to the fluid flow, volume penalties and affiliation (modeled as power law with exponent ν feedback as

$$\partial_h r_e \propto [\langle \Delta p_e^2 \rangle r_e^2 - \alpha] r_e - \beta \sum_{e'} F_{ee'} \Delta r_{ee'}^{-(\nu+1)} \quad (\text{C5})$$

with auxiliary coefficients $\chi, \alpha, \beta > 0$. For numerical evaluation we use the unit and parameter system of [2]: radii $r_e = Lr_e^*$, sink fluctuation $s_n = \mu s_n$, the conductivity $k_e = \eta^{-1}L^4\kappa_e$ and hence pressure $\Delta p_e = \frac{\mu\eta}{L^4}\Delta\Phi_e$ and the networks' edge surface distance $\Delta r_{ee'}^{-(\nu+1)} = L^{-(\nu+1)}\Delta r_{ee'}^{-(\nu+1)*}$. The ODEs (C5) can now be rescaled accordingly to the sink mean μ , providing us with the effective temporal response parameters $\lambda_0 = \chi\left(\frac{\mu\eta}{L^3}\right)^2$, the effective network coupling $\lambda_1 = \frac{\beta}{\pi\eta L^{\nu+1}}\left(\frac{\mu}{L^3}\right)^{-2}$, the effective volume penalty $\lambda_2 = \frac{4\alpha}{\pi\eta}\left(\frac{\mu}{L^3}\right)^{-2}$ and the effective flow-fluctuation $\lambda_3 = \frac{\sigma^2}{\mu^2}$. The coefficients λ_2, λ_3 are generally negligible as shown in [2, 28]. In Figure 8a and 8b we present the result for systematic parameter scans of affiliation

coupling λ_1 and fluctuation λ_3 in the case of repulsive ($\nu > 1$) and attractive interactions ($\nu < 0$). Here we present the state diagrams for minimal cut numbers ε_{12} , symmetry S and utilization ρ_{12} . Generally one finds the outline of the linkage transition to match the nullity transition discussed in [2]. Note that the adaptation parameters λ_i are chosen identically for all involved systems. It is interesting to note that the symmetry coefficient S seems particularly sensitive with regard to the regimes of the nullity transition, indicating different rates of acquiring reticulation in the networks probed. We assume this most likely to be an artifact of the chosen embedding though. Eventually, we would like to point out that the metric is applicable to even more sophisticated systems, e.g. intertwined networks which involve stimuli such as metabolite uptake [29].